



**HAL**  
open science

# Shear-induced pressure anisotropization and correlation with fluid vorticity in a low collisionality plasma

Daniele del Sarto, Francesco Pegoraro

► **To cite this version:**

Daniele del Sarto, Francesco Pegoraro. Shear-induced pressure anisotropization and correlation with fluid vorticity in a low collisionality plasma. *Monthly Notices of the Royal Astronomical Society*, 2018, 475 (1), pp.181-192. 10.1093/mnras/stx3083 . hal-01797828

**HAL Id: hal-01797828**

**<https://hal.science/hal-01797828>**

Submitted on 22 May 2018

**HAL** is a multi-disciplinary open access archive for the deposit and dissemination of scientific research documents, whether they are published or not. The documents may come from teaching and research institutions in France or abroad, or from public or private research centers.

L'archive ouverte pluridisciplinaire **HAL**, est destinée au dépôt et à la diffusion de documents scientifiques de niveau recherche, publiés ou non, émanant des établissements d'enseignement et de recherche français ou étrangers, des laboratoires publics ou privés.

# Shear-induced pressure anisotropization and correlation with fluid vorticity in a low collisionality plasma

Daniele Del Sarto<sup>1★</sup> and Francesco Pegoraro<sup>2★</sup>

<sup>1</sup>*Institut Jean Lamour, UMR 7198 CNRS - Université de Lorraine, F-54506 Vandoeuvre-lès-Nancy, France*

<sup>2</sup>*Dipartimento di Fisica, Università di Pisa, I-56127 Pisa, Italy*

Accepted 2017 November 26. Received 2017 November 26; in original form 2017 August 25

## ABSTRACT

The momentum anisotropy contained in a sheared flow may be transferred to a pressure anisotropy, both gyrotropic and non-gyrotropic, via the action of the fluid strain on the pressure tensor components. In particular, it is the traceless symmetric part of the strain tensor (*i.e.* the so-called shear tensor) that drives the mechanism, the fluid vorticity just inducing rotations of the pressure tensor components. This possible mechanism of anisotropy generation from an initially isotropic pressure is purely dynamical and can be described in a fluid framework where the full pressure tensor evolution is retained. Here, we interpret the correlation between vorticity and anisotropy, often observed in numerical simulations of solar wind turbulence, as due to the correlation between shear rate tensor and fluid vorticity. We then discuss some implications of this analysis for the onset of the Kelvin–Helmholtz instability in collisionless plasmas where a full pressure tensor evolution is allowed, and for the modelling of secondary reconnection in turbulence.

**Key words:** equation of state – instabilities – MHD – plasmas – turbulence – solar wind.

## 1 INTRODUCTION

Anisotropic, non-gyrotropic particle distributions are often directly observed in magnetospheric plasmas (Astudillo et al. 1996; Posner et al. 2003; Scudder & Daughton 2008; Scudder et al. 2012, 2015; He et al. 2015; Graham et al. 2017) and in Vlasov simulations of solar wind turbulence (Servidio et al. 2012; Perrone et al. 2013; Servidio et al. 2015; Franci et al. 2016b; Valentini et al. 2016) but the mechanism of generation of such anisotropies is still matter of investigation. Here, we further discuss a possible mechanism of purely dynamical nature, recently proposed in Del Sarto, Pegoraro & Califano (2016a), capable of generating both non-gyrotropic and gyrotropic pressure anisotropy from an initially isotropic plasma because of the action of the strain tensor related to a sheared flow.

The possibility of such anisotropic states in sufficiently diluted and/or warm plasmas is allowed as long as the particle collision time largely exceeds the characteristic time-scale of the dynamics. A well-known mechanism allowing (but not causing, *per se*) pressure anisotropization is the rapid particle gyromotion around a sufficiently strong magnetic field, whose presence breaks the spherical symmetry of an isotropic Maxwellian state into the ‘parallel’ and the ‘perpendicular’ directions to the field lines. Therefore, the first ex-

ample which has been provided of a plasma equilibrium anisotropic in pressure is the one associated with the gyrotropic, double adiabatic (or CGL) closure (Chew, Goldberger & Low 1956). However, it was soon noticed by Kaufman (1960) that inclusion of gyroviscous Finite–Larmor–Radius (FLR) corrections related to the components of the gradient velocity tensor breaks the gyrotropic symmetry of the CGL equilibrium, as it has been more recently shown to happen, for example, next to a reconnecting  $X$ -point (Brackbill 2011). The fact that in the presence of a velocity shear the kinetic equilibrium configurations are different from those predicted by an MHD model, and the role that the gyromotion and the polarity of the scalar product  $\mathbf{B} \cdot \boldsymbol{\omega}$  (with  $\mathbf{B}$  and  $\boldsymbol{\omega}$  being the magnetic field and fluid vorticity vectors, respectively) have in affecting these equilibria, was later pointed out by Cai, Storey & Neubert (1990). Non-gyrotropic CGL–FLR fluid equilibria have been then discussed by Cerri et al. (2013) and anisotropic equilibria in an extended fluid model including the full pressure tensor equation have been provided in Cerri et al. (2014).

*Per se*, the existence of such non-gyrotropic equilibrium solutions does not indicate how the anisotropy is generated. Here, we focus on the generation mechanism by assuming the collision rates to be negligible at the dynamical scale we consider. In particular, we are interested in discussing a possible explanation of the correlation frequently observed between pressure anisotropy and vorticity sheets forming at the boundary of convective cells in developed turbulence, in the light of the shear-driven anisotropization mechanism. While this point was already commented upon in Del

\* E-mail: daniele.del-sarto@univ-lorraine.fr (DDS); francesco.pegoraro@unipi.it (FP)

Sarto et al. (2016a) with reference, in particular, to the simulation results by Servidio et al. (2012) by pointing out that it is not the vorticity but rather the traceless rate of shear to act as a source mechanism for agyrotropy generation, some more recent articles (Franci et al. 2016b; Parashar & Matthaeus 2016; Valentini et al. 2016) have evidenced the correlation between vorticity and pressure anisotropy. In our previous work, however, we already noted that the correlation between gyrotropic anisotropy and vorticity evidenced by Franci et al. (2016b) supported the analysis we had presented. The purpose of this article is to address this latter point more explicitly. In doing so, we concur with the point of view more recently expressed by Yang et al. (2017a,b), whose numerical results in the kinetic regime appear to confirm the basis of the fluid modelling we present.

After recalling the physical model (Section 2), its typical parameters, and the dynamical features of the pressure tensor evolution (Section 3), we discuss how a vorticity sheet, such as those which are generated in turbulence or at the interface of two plasma flows in relative motion, is generally accompanied by a non-null symmetric part of the strain tensor (Section 4). We then show how this makes it possible to apply the analysis performed in Del Sarto et al. (2016a) in order to justify the generation of anisotropy near a vorticity sheet. This anisotropization mechanism may also inhibit the Kelvin–Helmholtz (KH) instability, whose occurrence may be prevented by the broadening of the initial velocity shear due to the full pressure tensor evolution (Section 5). In Section 6 we apply these results to explain the correlation between anisotropy and vorticity measured in simulations of 2D turbulence and we compare our interpretation with different interpretations available in the literature. Some implications and limitations of the shear-induced anisotropization mechanism for the description of Alfvénic turbulence are discussed in Section 7. In the Conclusions (Section 8), we summarize the results and we outline possible future developments.

## 2 MODEL EQUATIONS

We consider a two-fluid ‘extended’ MHD model with cold, massless electrons and we retain the contribution of the full ion pressure tensor  $\mathbf{\Pi}$  to the plasma dynamics, while disregarding the divergence of the heat flux in the pressure tensor evolution:

$$\frac{\partial n}{\partial t} + \nabla \cdot (n\mathbf{u}) = 0, \quad (1)$$

$$\frac{\partial \mathbf{u}}{\partial t} + \mathbf{u} \cdot \nabla \mathbf{u} = \Omega_c \frac{\mathbf{J} \times \mathbf{b}}{ne} - \frac{\nabla \cdot \mathbf{\Pi}}{mn}, \quad (2)$$

$$\frac{\partial \mathbf{\Pi}}{\partial t} + \nabla \cdot (\mathbf{u} \mathbf{\Pi}) + \mathbf{\Pi} \cdot \nabla \mathbf{u} + (\mathbf{\Pi} \cdot \nabla \mathbf{u})^T - \Omega_c (\mathbf{\Pi} \times \mathbf{b} + (\mathbf{\Pi} \times \mathbf{b})^T) = 0, \quad (3)$$

$$\mathbf{J} = \frac{c}{4\pi} \nabla \times \mathbf{B}, \quad (4)$$

$$\frac{\partial \mathbf{B}}{\partial t} = \nabla \times \left\{ \left( \mathbf{u} - \frac{\mathbf{J}}{ne} \right) \times \mathbf{B} \right\}. \quad (5)$$

Here,  $\Omega_c \equiv e|\mathbf{B}|/(mc)$  is the ion cyclotron frequency,  $\mathbf{b}$  the unit vector along the local magnetic field, the apex ‘ $T$ ’ is for matrix transpose, and  $\nabla \cdot (\mathbf{u} \mathbf{\Pi}) \equiv (\nabla \cdot \mathbf{u}) \mathbf{\Pi} + \mathbf{u} \cdot \nabla \mathbf{\Pi}$ .

## 3 TIME-SCALES AND DEFORMATIONS OF THE PRESSURE TENSOR

The evolution of the pressure tensor described by equation (3) is determined by the contribution of the two linear operators

$$\mathcal{L}_u(\mathbf{\Pi}) \equiv \nabla \cdot (\mathbf{u} \mathbf{\Pi}) + \mathbf{\Pi} \cdot \nabla \mathbf{u} + (\mathbf{\Pi} \cdot \nabla \mathbf{u})^T, \quad (6)$$

$$\mathcal{M}_B(\mathbf{\Pi}) \equiv \Omega_c (\mathbf{\Pi} \times \mathbf{b} + (\mathbf{\Pi} \times \mathbf{b})^T). \quad (7)$$

Their actions on  $\mathbf{\Pi}$  involve the time-scales  $\tau_H \equiv |\nabla \mathbf{u}|^{-1}$  and  $\tau_B \equiv \Omega_c^{-1}$ , respectively, whose ratio

$$\frac{\tau_B}{\tau_H} \equiv \frac{c_H}{c_A} \frac{d_i}{L_H} \quad (8)$$

depends on  $L_H \equiv |\mathbf{u}|/|\nabla \mathbf{u}|$ , typical shear length of the flow,  $c_H \equiv L_H/\tau_H \sim |\mathbf{u}|$ , characteristic magnitude of the fluid velocity,  $c_A$ , Alfvén velocity, and  $d_i \equiv c_A/\Omega_c$ , ion-skin depth. Depending on the ordering of the time-scales (8) with respect to those governing the dynamics of the other equations (1–5), it is possible to identify special limits leading to closure conditions, in which case the components of  $\mathbf{\Pi}$  can be related to the lower order moments,  $n$  and  $\mathbf{u}$ , and to the magnetic field.

In the present analysis, in order to focus on the shear-induced anisotropization process, we neglect the divergence of the heat flux, assuming it to be small. At least for the plasma dynamics perpendicular to the background magnetic field, this approximation is quite reasonable – see also Del Sarto, Pegoraro & Tenerani (2017) for a discussion of the role of the heat flux in the perpendicular propagation of linear modes, and Chust & Belmont (2006) for a general discussion on the adiabaticity hypothesis in fluid models.

In this article, we will specialize our analysis to a one-dimensional velocity shear configuration that depends on a single Cartesian coordinate perpendicular to the background magnetic field. This simplified configuration is sufficient to illustrate the mechanism of pressure anisotropy generation near a vorticity sheet, such as those encountered in 2D turbulence (geometry frequently adopted in kinetic and hybrid simulations of solar wind turbulence – see e.g. Franci et al. 2016b), and makes it possible to describe some processes at the solar wind/magnetosphere boundary at the flanks of the magnetopause, related to the onset of KH instabilities (Hasegawa et al. 1996). Extension to a higher dimension coordinate dependence requires a consistent description of the fluid dynamics parallel to the magnetic field. As evidenced by the linear analysis of Del Sarto et al. (2017), this is a delicate issue which will be examined in a future dedicated study.

### 3.1 Parameters of the system

A comparison of the characteristic amplitudes of each term of equations (1–5) shows that the non-linear dynamics of the whole set is ruled by three parameters,

$$\frac{\tau_B}{\tau_H}, \quad \frac{c_s}{c_A}, \quad \frac{c_A}{c_H}, \quad (9)$$

where  $c_s \equiv (2P_\perp/(nm_i))^{1/2}$  is the ‘sound’ velocity evaluated with respect to an ion pressure, initially gyrotropic with respect to the local magnetic field  $\mathbf{B}$ . The second and third parameters arise from the comparison of the two force terms in the momentum equation (2) and from the contribution of the convection terms  $\sim \mathbf{u} \cdot \nabla$  in equations (1–3). Even if  $c_A/c_H$  formally disappears in a linear mode analysis of the waves propagating in the system, it still contributes to the definition of  $\tau_B/\tau_H$  when we choose  $L_H/d_i$  as an

independent parameter. This suggests to identify

$$\ell \equiv \frac{L_H}{d_i}, \quad \beta \equiv \left(\frac{c_s}{c_A}\right)^2, \quad M_A \equiv \frac{c_H}{c_A}, \quad (10)$$

as the three fundamental independent parameters descriptive of both the linear and non-linear properties of the system, where we have adopted the standard notation for the plasma  $\beta$  (evaluated for the ion pressure only) and for the Alfvén-Mach number,  $M_A$ . We then recall that either  $\beta$  or  $M_A$  can be replaced by the sonic Mach number

$$M_s \equiv \frac{c_H}{c_s} = \frac{M_A}{\sqrt{\beta}}. \quad (11)$$

### 3.2 Deformations of the pressure tensor

In order to summarize the discussion of the pressure tensor evolution given in Del Sarto et al. (2016a), we recast equation (3) by expressing the action on  $\Pi$  of the *strain tensor*  $\Sigma \equiv \nabla u_i$  and of the magnetic field in terms of matrix operators. Thus, we split (see e.g. Batchelor 1967, Section 2.3) the strain tensor in terms of its traceless symmetric part, that is the *incompressible rate of shear*  $\mathbf{D}$ , of its anti-symmetric part, that is the *vorticity tensor*  $\mathbf{W}$ , and of the contribution from the *isotropic compression*  $C\mathbf{I}$  (related to  $\nabla \cdot \mathbf{u}$  by a minus sign as  $\nabla \cdot \mathbf{u} = -3C$ ):

$$\underbrace{\nabla u}_{\Sigma} = \underbrace{\frac{1}{3}(\nabla \cdot \mathbf{u})\mathbf{I}}_{-C\mathbf{I}} + \underbrace{\frac{1}{2} \left[ \nabla u + (\nabla u)^T - \frac{2}{3}(\nabla \cdot \mathbf{u})\mathbf{I} \right]}_{\mathbf{D}} + \underbrace{\frac{1}{2} [\nabla u - (\nabla u)^T]}_{\mathbf{W}}. \quad (12)$$

irrotational strain tensor ( $S$ )

In tensor notation, which we will also use in the following, the above equation reads

$$\underbrace{\frac{\partial u_j}{\partial x_i}}_{\Sigma_{ij}} = \underbrace{\frac{1}{3} \left( \frac{\partial u_k}{\partial x_k} \right) \delta_{ij}}_{-C\delta_{ij}} + \underbrace{\frac{1}{2} \left[ \left( \frac{\partial u_j}{\partial x_i} + \frac{\partial u_i}{\partial x_j} \right) - \frac{2}{3} \left( \frac{\partial u_k}{\partial x_k} \right) \delta_{ij} \right]}_{D_{ij}} + \underbrace{\frac{1}{2} \left( \frac{\partial u_j}{\partial x_i} - \frac{\partial u_i}{\partial x_j} \right)}_{W_{ij}}. \quad (13)$$

irrotational strain tensor ( $S_{ij}$ )

Isotropic compressions and the incompressible rate of shear contribute to the irrotational strain tensor  $S_{ij} \equiv D_{ij} - C\delta_{ij}$ , while  $W_{ij}$  is related to the fluid vorticity  $\boldsymbol{\omega} \equiv \nabla \times \mathbf{u}$  by duality,  $\omega_i = \varepsilon_{ijk}W_{jk}$ , where  $\varepsilon_{ijk}$  is the usual Levi-Civita symbol.

By analogy, we define the matrix  $\mathbf{B}$  related by duality to the local magnetic field  $\mathbf{B}$  according to  $B_{ij} \equiv \Omega_c \varepsilon_{ijm} b_m$ , and expressing gyrotropic rotations. Introducing the commutator  $[\cdot, \cdot]$  and anti-commutator  $\{\cdot, \cdot\}$  between matrices, equation (3) can be then rewritten in a compact form as

$$\frac{\partial \Pi}{\partial t} + \mathbf{u} \cdot \nabla \Pi = [\mathbf{B} + \mathbf{W}, \Pi] - \{\mathbf{D}, \Pi\} + 5C\Pi. \quad (14)$$

This expression shows that  $\mathbf{B}$  and  $\mathbf{W}$  combine to generate rotations of  $\Pi$  around the magnetic field direction and the vorticity direction, respectively. Isotropy of  $\Pi$  in the plane perpendicular to  $\mathbf{B}$  (or to  $\boldsymbol{\omega}$ ) implies the vanishing of the commutator  $[\mathbf{B}, \Pi]$  (or  $[\mathbf{W}, \Pi]$ ). When the magnetic field and the vorticity vector are locally aligned,

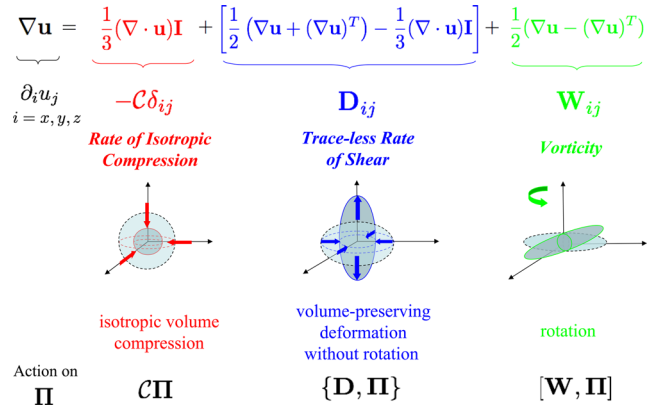


**Figure 1.** Sketch of the possible deformations induced by the strain tensor  $\nabla \mathbf{u}$  on the pressure tensor  $\Pi$ , whose principal axes define the shape of an ellipsoid. In the three diagrams, we have represented the examples:  $C > 0$  acting on an isotropic  $\Pi$  (red);  $\mathbf{D}$  compressing an ellipsoidal (gyrotropic)  $\Pi$  along the two initial major axes (blue); and  $\mathbf{W}$  having the rotation axis parallel to one of the minor axes of an ellipsoidal (gyrotropic)  $\Pi$ .

for example along  $z$ , by considering the local spatial dependence of the cyclotron frequency,  $\Omega_c(x)$ , and of the modulus of the vorticity,  $\omega(x)$ , the local gyration frequency  $\Omega'(x)$  around the magnetic lines is increased by the vortical dynamics,  $|\Omega'(x)| = |\Omega_c(x)| + |\omega(x)|$ , when  $\mathbf{B} \cdot \boldsymbol{\omega} > 0$ , whereas it is decreased,  $|\Omega'(x)| = |\Omega_c(x)| - |\omega(x)|$ , when  $\mathbf{B} \cdot \boldsymbol{\omega} < 0$ . This spatial ‘asymmetry’ related to the sign of  $\mathbf{B} \cdot \boldsymbol{\omega}$  plays a key role in the forced solutions discussed in Section IV of Del Sarto et al. (2016a) obtained by assuming the velocity and magnetic field fixed in time: an initial sheared velocity profile transfers the spatial inhomogeneity in an anisotropic way to the components of the pressure tensor, with a rate which, when  $\mathbf{B}$  is spatially uniform, is exponential for  $\Omega_c \Omega'(x) < 0$  and periodic in time for  $\Omega_c \Omega'(x) > 0$ . Moreover, the  $\mathbf{B} \cdot \boldsymbol{\omega}$ -related asymmetry is at the basis of the asymmetric behaviour which may influence the KH dynamics in presence of magnetic field (Huba 1996), as it is well known to happen at the flanks of the terrestrial magnetosphere (Hasegawa et al. 1996). We will return to this subject in Section 5.

The other feature we will focus on is the generation of pressure anisotropy by the symmetric term  $\{\mathbf{D}, \Pi\}$  of equation (14).

The deformations of  $\Pi$  related to each of the r.h.s. terms of equation (13) are summarized in Fig. 1.

#### 3.2.1 Gyrotropic anisotropy in a double adiabatic closure

The most commonly used notion of the term ‘anisotropy’ in plasma literature refers to the gyrotropic CGL-type, double adiabatic anisotropy  $P_{\parallel}/P_{\perp}$  (see e.g. Schekochihin et al. 2008), where  $P_{\parallel}$  and  $P_{\perp}$  are, respectively, the parallel and perpendicular pressure to the local magnetic field, sufficiently intense to grant the CGL, gyrotropic form of the pressure tensor (Chew et al. 1956):

$$\Pi_{ij}^{\text{CGL}} \equiv P_{\perp} \delta_{ij} + (P_{\parallel} - P_{\perp}) b_i b_j. \quad (15)$$

When the cyclotron frequency is the dominant inverse time-scale of equation (5) so that  $\tau_B/\tau_H \ll 1$ ,  $\Pi_{ij}^{\text{CGL}}$  is indeed the leading order solution in the expansion of  $\Pi$  that satisfies  $\mathcal{M}_B(\Pi) = [\mathbf{B}, \Pi] = 0$ . Thanks to the lower time resolution required, the gyrotropic anisotropy is typically easier to be measured than pressure agyrotropy, both by satellites and in numerical simulations, and in gyro-averaged descriptions is obviously the dominant pressure anisotropy which can be observed. This anisotropy follows from the two

equations which are obtained by, respectively, contracting equation (14) with  $\delta_{ij}$  (i.e. by taking the trace) and with  $b_i b_j$  (i.e. by taking the projection along the local direction of  $\mathbf{B}$ ). For a generic form of  $\mathbf{\Pi}$ , we have  $\text{tr}\{[\mathbf{B} + \mathbf{W}, \mathbf{\Pi}]\} = 0$  and  $[\mathbf{B}, \mathbf{\Pi}]_{ij} b_i b_j = 0$  because of symmetry. Then, expanding the pressure tensor as  $\mathbf{\Pi} = \mathbf{\Pi}^{\text{CGL}} + \mathbf{\Pi}^{(1)} + \dots$  and ordering  $\partial_t \sim u_k \partial_k \sim \|\mathbf{D}\| \sim \|\mathbf{W}\| \sim \tau_H^{-1}$ , we find that the projected equations at the leading order  $o(\tau_B/\tau_H)$  are:

$$\frac{\partial}{\partial t}(2P_{\perp} + P_{\parallel}) + u_k \frac{\partial}{\partial x_k}(2P_{\perp} + P_{\parallel}) - 5\mathcal{C}(2P_{\perp} + P_{\parallel}) + 2(P_{\parallel} - P_{\perp})D_{lk} b_l b_k = 0, \quad (16)$$

$$\frac{\partial P_{\parallel}}{\partial t} + u_k \frac{\partial P_{\parallel}}{\partial x_k} - 5\mathcal{C}P_{\parallel} + 2P_{\parallel}D_{lk} b_l b_k = 0. \quad (17)$$

The diagonal form of  $\mathbf{\Pi}_{ij}^{\text{CGL}}$  has made the vorticity contribution disappear from the equation for  $P_{\parallel}$  too, since  $[\mathbf{W}, \mathbf{\Pi}^{\text{CGL}}]_{ij} b_i b_j = 0$  because of symmetry. Also note that symmetry grants  $[\mathbf{B}, \mathbf{\Pi}^{(1)}]_{ij} \delta_{ij} = 0$  and  $[\mathbf{B}, \mathbf{\Pi}^{(1)}]_{ij} b_i b_j = 0$ , which makes the set (16–17) closed with respect to the zeroth-order expansion of  $\mathbf{\Pi}$ . Obtaining the equation for  $P_{\perp}$  is then straightforward,

$$\frac{\partial P_{\perp}}{\partial t} + u_k \frac{\partial P_{\perp}}{\partial x_k} - 5\mathcal{C}P_{\perp} - P_{\perp}D_{lk} b_l b_k = 0. \quad (18)$$

A more customary form of the ‘generalized CGL-type’ equations (17–18) – cf., e.g., App. B of Del Sarto et al. (2017) – is obtained by expressing  $\mathcal{C}$  and  $D_{ij}$  as defined in equation (13). Equations (17–18) make it manifest that the gyrotropic anisotropy allowed by this closure condition follows from the different compression on the components  $P_{\perp}$  and  $P_{\parallel}$ , which are due to the projection of  $\mathbf{D}$  along the local magnetic field. For  $\mathbf{D} = 0$ , the evolution of both  $P_{\perp}$  and  $P_{\parallel}$  is adiabatic (with polytropic index 5/3) and becomes isobaric if  $\mathcal{C} = 0$ , too.

The  $\mathbf{D} = 0$  case is relevant, for instance, to von Karman flow experiments, such as those discussed by Plihon et al. (2015), in which a cylindrical plasma is set in motion by a dominant eddy flow with  $\mathbf{B} \times \boldsymbol{\omega} = 0$ . In this case, a non-isotropic, gyrotropic pressure evolution would be allowed at the  $(\tau_B/\tau_H)^0$  order of validity of equations (17–18) only if the gradients of the heat flux were retained.

In the more general  $\mathbf{D} \neq 0$  case, the CGL-type closure may also account for a non-gyrotropic pressure anisotropy once FLR corrections of the order of  $o(\tau_B/\tau_H)$  are retained to describe the  $\mathbf{\Pi}^{(1)}$  components (Kaufman 1960; Cerri et al. 2013). These corrections are obtained by balancing the non-null contributions of  $[\mathbf{B}, \mathbf{\Pi}^{(1)}]$  with the remaining components of equation (14). It results, however, that these extended model equations fail to provide a consistent dispersion of magnetoacoustic modes (MacMahon 1965; Del Sarto et al. 2017): the full pressure tensor evolution must be retained when the hypothesis  $\tau_B/\tau_H \ll 1$  is relaxed, and a more accurate FLR expansion accounting for the contribution of higher order moments should be retained for values of  $\beta \sim 1$  (Mikhailovskii and Smolyakov 1985; Sulem & Passot 2015; Del Sarto et al. 2017).

We conclude by recalling that equations (17–18) assume a particularly simple form when they are coupled to the continuity and ideal Ohm’s law, which provides the standard double adiabatic form

$$\frac{d}{dt} \left( \frac{P_{\perp}}{n|\mathbf{B}|} \right) = 0, \quad \frac{d}{dt} \left( \frac{P_{\parallel}|\mathbf{B}|^2}{n^3} \right) = 0, \quad (19)$$

where  $d/dt \equiv \partial_t + \mathbf{u} \cdot \nabla$ , or when gradients are assumed to be purely parallel or purely perpendicular to the magnetic field. In these latter cases, polytropic closures with different indices for  $P_{\perp}$  and  $P_{\parallel}$  are obtained from equations (17–18). With obvious notation,

these correspond to  $T_{\parallel} \propto n^2$  and  $T_{\perp} = \text{constant}$  (i.e. to polytropic indices  $\Gamma_{\parallel} = 3$  and  $\Gamma_{\perp} = 1$ ) when spatial gradients are approximately parallel to  $\mathbf{B}$ , and to  $T_{\parallel} = \text{constant}$  and  $T_{\perp} \propto n$  (i.e. to polytropic indices  $\Gamma_{\parallel} = 1$  and  $\Gamma_{\perp} = 2$ ) when spatial gradients are approximately perpendicular to  $\mathbf{B}$ .

The latter case is relevant, for example, to the solar wind: an interpretation mechanism for the main features of the gyrotropic anisotropy at a given radial distance  $R$  from the Sun can be provided (Matteini et al. 2012) by using the standard double adiabatic equations in the limit of negligible parallel gradients of the solar wind velocity, once we estimate  $n \propto R^{-2}$  and we consider a power-law scaling in  $R$  for the amplitude of the magnetic field components. For example,  $|\mathbf{B}| \propto R^{-2}$  can be assumed for a strictly radial magnetic field, whereas a scaling  $\propto R^{-1}$  should be further considered for the tangential magnetic component in Parker’s spiral magnetic field model.

### 3.2.2 Gyrotropic and non-gyrotropic anisotropy in a planar flow

Anisotropy, of both gyrotropic and non-gyrotropic type, is naturally referred to the *local principal axes* of  $\mathbf{\Pi}$ . In the  $\mathbf{B} \times \boldsymbol{\omega} = 0$  case of interest here, one of these axes, which we relate to the eigenvalue  $\Pi_{\parallel}$ , will be aligned to the common axis of rotation of both  $\mathbf{B}$  and  $\mathbf{W}$ . Naming  $P_1$  and  $P_2$  the eigenvalues corresponding to the other two principal axes of the pressure tensor, its agyrotropy, that is its non-gyrotropic anisotropization, can be quantified as

$$A^{\text{ng}} \equiv \frac{P_1 - P_2}{P_1 + P_2}, \quad (20)$$

whereas its gyrotropic anisotropization is given by

$$A^{\text{gyr}} \equiv \frac{2P_{\parallel}}{P_1 + P_2}. \quad (21)$$

From now on, we restrict to a geometry where the magnetic field is along  $z$ , coordinate with respect to which we assume translational invariance ( $\partial_z = 0$ ). We will consider the  $u_x$  and  $u_y$  components only, since the flow in the  $(x, y)$  plane results to be decoupled from the  $u_z$  components, while the  $\mathbf{B} \times \boldsymbol{\omega} = 0$  condition is verified at any time. The strain tensor is now a  $2 \times 2$  matrix,  $(\nabla \mathbf{u})_{\perp}$ , written in tensor notation as  $\partial_i u_j$  with the latin indices which from now on read  $i, j = x, y$ . Then, the isotropic *volume compression* coefficient  $\mathcal{C}$  becomes an isotropic *surface compression* coefficient defined as

$$\mathcal{C}_{\perp} \equiv -\frac{1}{2} \frac{\partial u_k}{\partial x_k} \quad (k = x, y). \quad (22)$$

The traceless rate of shear  $\mathbf{D}$  of equation (13), which now becomes a  $2 \times 2$  matrix,  $\mathbf{D}_{\perp}$ , related to non-isotropic surface compressions, should be accordingly re-defined as

$$D_{\perp,ij} \equiv \frac{1}{2} \left[ \frac{\partial u_i}{\partial x_j} + \frac{\partial u_j}{\partial x_i} \right] + \mathcal{C}_{\perp} \delta_{ij} \quad (i, j = x, y). \quad (23)$$

In this geometry, the pressure tensor has a diagonal block form,  $\mathbf{\Pi} = \mathbf{\Pi}_{\perp} + P_{\parallel} \mathbf{b}\mathbf{b}$ , and its evolution equation in matrix form, which replaces equation (14), rewrites as

$$\frac{d\mathbf{\Pi}}{dt} = [\mathbf{B}_{\perp} + \mathbf{W}_{\perp}, \mathbf{\Pi}] - \{\mathbf{D}_{\perp}, \mathbf{\Pi}\} + 4\mathcal{C}_{\perp} \mathbf{\Pi}, \quad (24)$$

where the symbol ‘ $\perp$ ’ labels the  $x - y$  components of the matrices  $\mathbf{B}$  and  $\mathbf{W}$  previously defined in equations (12–14) and  $d/dt$  is the total time derivative already introduced in equations (19). Using the equation for the trace of  $\mathbf{\Pi}_{\perp}$ , which can be directly deduced from

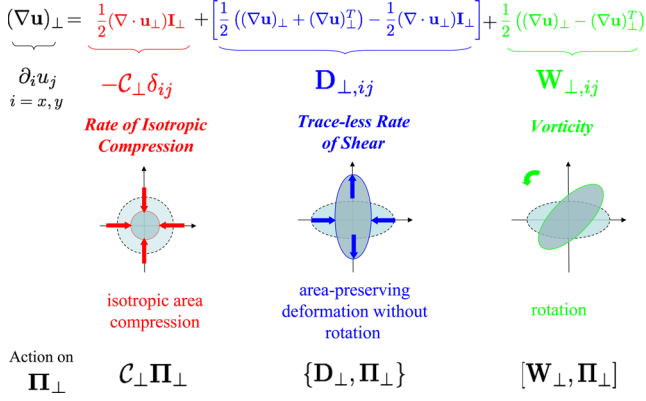


**Figure 2.** Sketch of the possible deformations induced by the  $2 \times 2$  strain tensor  $(\nabla \mathbf{u})_{\perp}$  on the pressure tensor  $\Pi_{\perp}$ , whose principal axes define the shape of an ellipse in the  $(x, y)$  plane. Examples in the diagrams:  $C_{\perp} > 0$  acting on an isotropic  $\Pi_{\perp}$  (red);  $D_{\perp}$  compressing an agyrotropic  $\Pi_{\perp}$  along its major axis (blue);  $W_{\perp}$  rotating an agyrotropic  $\Pi_{\perp}$  in the  $(x, y)$  plane (green).

the previous one,

$$\frac{d}{dt} \text{tr}(\Pi_{\perp}) = -2\text{tr}(\mathbf{D}_{\perp} \Pi_{\perp}) + 4C_{\perp} \text{tr}(\Pi_{\perp}), \quad (25)$$

the equation for the non-gyrotropic part of the perpendicular matrix component  $\Pi_{\perp}$ ,  $\Pi_{\perp}^{\text{ng}} \equiv \Pi_{\perp} - \text{tr}\{\Pi_{\perp}\}\mathbf{I}_{\perp}/2$ , reads

$$\frac{d\Pi_{\perp}^{\text{ng}}}{dt} = [\mathbf{B}_{\perp} + \mathbf{W}_{\perp}, \Pi_{\perp}^{\text{ng}}] - \{\mathbf{D}_{\perp}, \Pi_{\perp}^{\text{ng}}\} + 4C_{\perp} \Pi_{\perp}^{\text{ng}} + \mathbf{I}_{\perp} \text{tr}(\mathbf{D}_{\perp} \Pi_{\perp}^{\text{ng}}) - \mathbf{D}_{\perp} \text{tr}(\Pi_{\perp}^{\text{ng}}). \quad (26)$$

It shows with its last r.h.s. term that a non-null rate of shear can generate agyrotropy on a time-scale  $\tau_{an} \sim \|\mathbf{D}_{\perp}\|^{-1}$  from an initial isotropic state. The evolution of the parallel component  $P_{\parallel} = \Pi_{ij}b_i b_j$ , calculated by projecting equation (14) on  $b_i b_j$  and already written in the form of equation (17) for a more general  $3 \times 3$  matrix expression of the strain rate  $\mathbf{D}$ , assumes a more trivial form of a polytropic with index 2 in this  $\mathbf{B} \times \boldsymbol{\omega} = 0$  case where  $\{\mathbf{D}_{\perp}, \Pi\}_{ij}b_i b_j = 0$ ,

$$\frac{dP_{\parallel}}{dt} = 4C_{\perp} P_{\parallel}. \quad (27)$$

The deformations related to the strain tensor, specialized to a two-dimensional geometry, acting on  $\Pi_{\perp}$  are schematized in Fig. 2.

#### 4 ANISOTROPIZATION NEAR A ‘VORTICITY SHEET’

We apply the shear-induced mechanism of anisotropization to large aspect ratio vorticity sheets, such as those generated at the boundary of a convective cell in turbulence or at the interface of two fluids in relative motion one with respect to each other (consider, for example, the magnetopause boundary with the solar wind). The main point we make here is that such a sheared flow corresponds to a traceless rate of shear of characteristic amplitude comparable to the fluid vorticity, that is  $\|\mathbf{D}_{\perp}\| \sim \|\mathbf{W}_{\perp}\|$ .

Consider a vorticity sheet characterized by a large-scale separation between its length extension, say  $L$ , and its thickness, say  $\delta$ . The assumption  $\delta \ll L$  means that  $|\partial_{\delta} u_L| \gg |\partial_L u_{\delta}|$ , with ‘ $\partial_{\delta}$ ’ and ‘ $\partial_L$ ’ expressing the gradient across and along the vorticity sheet, respectively. We can thus assume a planar configuration by approximating the vorticity sheet as a 1D structure of infinite length  $L$  with

respect to the scale of variation across its thickness. Taking  $y$  to be the coordinate along the vorticity sheet, we model the latter by assuming an initial velocity profile  $\mathbf{u}^0 = (0, u_y^0(x/\delta), 0)$ , sheared with respect to a coordinate  $x$  over a length-scale  $L_H \equiv \delta \ll L$ , and we will consider its evolution on spatial intervals in  $x$  that remain much smaller than  $L$ . This initial flow is incompressible ( $C_{\perp} = 0$ ) and has a rotational component corresponding to a vorticity  $\boldsymbol{\omega} = (0, 0, \partial_x u_y^0(x))$ . Thus, at  $t = 0$ , the components of  $\mathbf{D}_{\perp}$  and  $\mathbf{W}_{\perp}$  read

$$\mathbf{D}_{\perp} \equiv \begin{pmatrix} 0 & \omega_z/2 \\ \omega_z/2 & 0 \end{pmatrix}, \quad \mathbf{W}_{\perp} \equiv \begin{pmatrix} 0 & \omega_z/2 \\ -\omega_z/2 & 0 \end{pmatrix}, \quad (28)$$

where  $\omega_z \equiv \partial_x u_y^0(x)$  has the characteristic amplitude

$$\omega_z \sim \frac{c_H}{L_H} \sim \frac{d_i}{\delta} M_A \Omega_c. \quad (29)$$

This  $\mathbf{u}^0 = (0, u_y^0(x/\delta), 0)$  sheared flow, besides representing a potentially KH-unstable configuration, as we will discuss in Section 5, can be seen also as the limit of a 2D ‘stretched’ eddy-like incompressible flow of the kind  $\mathbf{u}(x, y) = \mathbf{e}_z \times \nabla \varphi(x, y)$ , with the stream function having contour lines  $(x/\delta)^2 + (y/L)^2 = \text{constant}$ . In this case, the error made is in neglecting additional terms which are only  $\delta/L$  smaller than the dominant elements in the off-diagonal components of both  $\mathbf{D}_{\perp}$  and  $\mathbf{W}_{\perp}$ , which are of the order of  $c_H/\delta$ . Examples of more complex flows with  $\mathbf{D}_{\perp} = 0$  and non-null vorticity are discussed in Appendix A.

The simplification of assuming both the vorticity and magnetic field axes to be approximately parallel (to the  $z$ -axis), and which, as already noted, allows us to maintain a fully planar evolution of the fluid in the  $(x, y)$  plane, implies negligible (formally zero) in-plane components of the magnetic field and therefore restricts the regimes of Alfvénic turbulence with which this analysis can be compared quantitatively. On the other hand, it excludes the well-known stabilizing effect of an in-plane magnetic field for the KH instability, therefore allowing for a better comparison with the ‘stabilizing effect’ related to a full pressure tensor evolution that may prevent the onset of the KH instability in this configuration, as we will discuss in Section 5.

As stated by equations (20–21), the local non-gyrotropic and gyrotropic anisotropies are related to the eigenvalues  $P_1, P_2$ , and  $P_{\parallel}$  of the pressure tensor. Choosing  $A^{\text{ng}}$  to be positive defined and  $P_{\parallel}$  to be the largest eigenvalue of  $\Pi_{\perp}$ , this relation can be expressed in a matrix form as

$$\begin{pmatrix} P_1 & 0 & 0 \\ 0 & P_2 & 0 \\ 0 & 0 & P_{\parallel} \end{pmatrix} = \frac{\text{tr}\{\Pi_{\perp}\}}{2} \begin{pmatrix} 1 + A^{\text{ng}} & 0 & 0 \\ 0 & 1 - A^{\text{ng}} & 0 \\ 0 & 0 & A^{\text{gyr}} \end{pmatrix}. \quad (30)$$

Since the traces of  $\Pi$  and  $\Pi_{\perp}$  are invariant with respect to the rotation around the  $z$ -axis which brings  $\Pi$  to the local diagonal form (30), it is possible to express  $A^{\text{ng}}$  and  $A^{\text{gyr}}$  in terms of the coordinate components of  $\Pi$ . In particular,  $P_{\parallel} = \Pi_{zz}$  and  $P_{\perp} = \text{tr}\{\Pi_{\perp}\}/2 = (\Pi_{xx} + \Pi_{yy})/2$ . Equations (20–21) then become

$$A^{\text{ng}} = \frac{\sqrt{(\text{tr}\{\Pi_{\perp}\})^2 - 4 \det\{\Pi_{\perp}\}}}{\text{tr}\{\Pi_{\perp}\}}, \quad A^{\text{gyr}} = \frac{2P_{\parallel}}{\text{tr}\{\Pi_{\perp}\}}. \quad (31)$$

Naming  $\theta(x, t)$  the angle between the principal axes of  $\Pi_{\perp}$  and its local components in the Cartesian reference frame, i.e. the angle of the local rotation around  $z$  which brings  $\Pi$  to the diagonal form (30) according to  $2\Pi_{xy} = A^{\text{ng}} \text{tr}\{\Pi_{\perp}\} \sin 2\theta$  and  $\Pi_{xx} - \Pi_{yy} = A^{\text{ng}} \text{tr}\{\Pi_{\perp}\} \cos 2\theta$ , and naming  $\phi(x, t)$  the angle of the analogous

rotation which brings  $\mathbf{D}_\perp$  to the form

$$\begin{pmatrix} D_\perp & 0 \\ 0 & -D_\perp \end{pmatrix} \quad (32)$$

according to  $D_{xy} = D \sin 2\phi$  and  $D_{xx} - D_{yy} = 2D \cos 2\phi$ , it is possible to write the equations for the time evolution of  $A^{\text{ng}}$  and  $A^{\text{gyr}}$ . The former has been provided in Del Sarto et al. (2016a)

$$\frac{dA^{\text{ng}}}{dt} = 2D_\perp [(A^{\text{ng}})^2 - 1] \cos[2(\theta - \phi)]. \quad (33)$$

A straightforward derivation of the equation above follows from differentiating  $(A^{\text{ng}})^2$  as given by equation (31) while using  $\det\{\mathbf{\Pi}_\perp\} = ((\text{tr}\{\mathbf{\Pi}_\perp\})^2 - \text{tr}\{\mathbf{\Pi}_\perp \mathbf{\Pi}_\perp\})/2$  and equations (25–26, 31), and noting that  $\text{tr}\{\mathbf{D}_\perp \mathbf{\Pi}_\perp\} = A^{\text{ng}} D_\perp \text{tr}\{\mathbf{\Pi}_\perp\} \cos[2(\theta - \phi)]$ .

An analogous equation for  $A^{\text{gyr}}$  can be obtained by using  $A^{\text{gyr}} = 2(\text{tr}\{\mathbf{\Pi}\}/\text{tr}\{\mathbf{\Pi}_\perp\} - 1)$ , the trace of equation (24), and equation (25):

$$\frac{dA^{\text{gyr}}}{dt} = 2D_\perp A^{\text{gyr}} A^{\text{ng}} \cos[2(\theta - \phi)]. \quad (34)$$

Equations (33–34) state that both  $A^{\text{ng}}(x, t)$  and  $A^{\text{gyr}}(x, t)$  increase in time at a rate which is maximum when the major (minor) principal axes of  $\mathbf{\Pi}_\perp$  and  $\mathbf{D}_\perp$  are de-phased by an angle  $\pi/2$ . Neither  $\mathcal{C}_\perp$  nor  $\mathbf{W}_\perp$  contributes to the evolution of  $A^{\text{ng}}$  and  $A^{\text{gyr}}$ . We now identify the maximum anisotropization rate of both  $A^{\text{ng}}$  and  $A^{\text{gyr}}$  to be  $\tau_{\text{an}}^{-1} \sim \|\mathbf{D}_\perp\| = D_\perp$ , hence from equations (28–29) it follows  $\tau_{\text{an}}^{-1} \sim \|\mathbf{D}_\perp\| = c_H/L_H$  close to a vorticity sheet.

We can therefore quantify the anisotropization mechanism near a vorticity sheet given as an initially steady configuration (for instance, as the result of a local force balance condition) by considering the numerical example analysed in Del Sarto et al. (2016a), with parameters  $\beta = 1$ ,  $\ell = 1$  ( $\delta = d_i$ ), and  $M_A = 1$  [relevant, for example, to the magnetospheric environment (Nakamura, Hasegawa & Shinohara 2010)], with an initial isotropic pressure  $\Pi_{ij}^0 = c_A^2/2\delta_{ij}$  and with a velocity profile  $u_y^0(x) = c_A \tanh(x/d_i)/\cosh^2(x/d_i)$ , which corresponds to a Fourier spectrum peaked at  $k_x d_i < 1$ . The contour-plots of Fig. 3, obtained by integrating with a spectral code, using a third-order Runge–Kutta algorithm for the time advancement, the full set of equations (1–5) initialized with the profiles above, show that a relatively long-standing anisotropy both non-gyrotropic (frame a) and gyrotropic (frame b) is generated after an initial rapid transient – cf. for a comparison the corresponding shade-surface plot in fig. 7a and b of Del Sarto et al. (2016a). The fact that  $A^{\text{gyr}}$  and  $A^{\text{ng}}$  appear correlated to *both* a traceless rate of shear and to a fluid vorticity is evidenced by frame c, where the contour-plot of  $\omega_z$  is shown (cf. equations 28).

## 5 AGYROTROPY AND STABILITY OF A VORTICITY SHEET

The previous analysis has been performed by assuming an initially given current sheet, which acts as a source for the anisotropy. Such a vorticity sheet would be in an equilibrium configuration in an isotropic MHD plasma, but it is not in equilibrium when a full pressure tensor evolution is accounted for (Cerri et al. 2014; Del Sarto et al. 2016a). When described by equations (1–5), the current sheet evolves [i.e.  $D_\perp(x, t)$  and  $\phi(x, t)$  of equations (33–34) change in time]. However, as evidenced by Fig. 3, such an evolution may be relatively slow with respect to the rate of anisotropization, which justifies the approach we have previously developed.

The pressure tensor evolution induces a progressive broadening of the vorticity sheet, which, for a sheared velocity

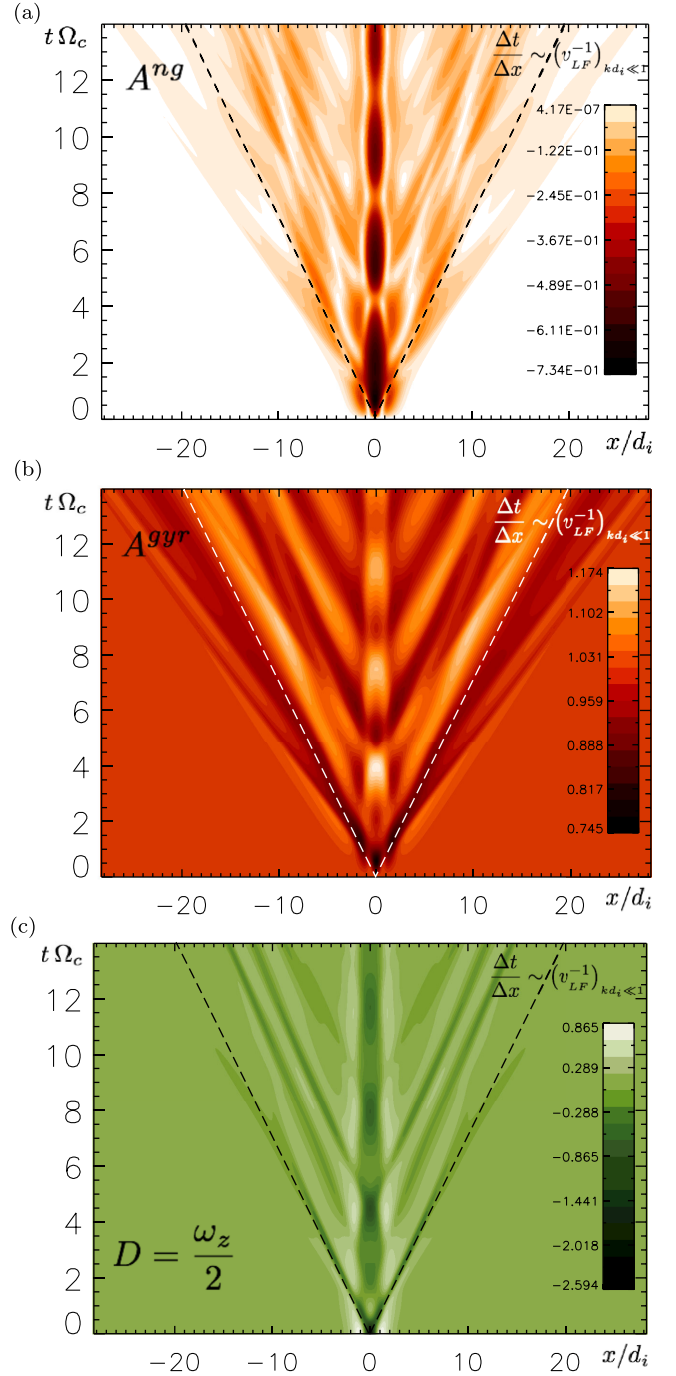


**Figure 3.** From the top to bottom: amplitude, with respect to  $x$  (abscissa) and  $t$  (ordinate) of the non-gyrotropic anisotropy  $A^{\text{ng}}$  (a), of the gyrotropic anisotropy  $A^{\text{gyr}}$  (b), and of the eigenvalue  $D$  of the shear rate matrix (c), which here coincides with half the fluid vorticity  $\omega_z = \partial_x u_y$  (cf. equation 28). The simulation has been initialized with  $\Pi_{ij}^0 = \delta_{ij}/2$ ,  $\mathbf{u}^0 = (0, u_y^0, 0)$  with  $u_y^0(x) = \tanh(x/d_i)/\cosh^2(x/d_i)$ ,  $\mathbf{B}^0 = (0, 0, 1)$ , and  $\beta = 1$ ,  $\ell = 1$ ,  $M_A = 1$ . The dashed lines represent the slopes of  $\Delta t/\Delta x = \pm 1/\sqrt{2}$ , here drawn for reference, since they correspond to the approximate phase velocities  $v_{LF}$  in the limit  $kd_i \ll 1$ . The contour-plots (a) and (b) correspond to the shade-surface plot of figs 7a and b of Del Sarto et al. (2016a).

profile with spectral density peaked at  $k_x d_i < 1$ , occurs on a time-scale  $\sim (k_x (c_A^2 + c_s^2)^{1/2})^{-1}$ . At  $d_i \sim \rho_i$ , (that is for  $M_A \sim M_s$ ) and  $L_H \sim d_i$ , as is the case for the numerical example of Fig. 3, this ‘broadening time’ is by a factor  $c_H / (c_A k_x d_i \sqrt{2}) = M_A / (k_x d_i \sqrt{2})$  longer than the anisotropization time  $\tau_{\text{an}} \sim d_i / c_H$ . This estimate can be obtained from a heuristic model, in which the vorticity sheet is treated as if it were an initial perturbation on an isotropic equilibrium, homogeneous in density and with zero vorticity.

The linear analysis detailed in Del Sarto et al. (2017) shows that a low-frequency (LF) branch, corresponding to a fast magnetoacoustic wave, and a high-frequency (HF) branch, corresponding to a generalized, non-quasi-electrostatic  $m = 2$  ion-Bernstein wave, can be excited. Based on this analysis, a given vorticity sheet with spectral density peaked at  $k_x d_i < 1$  excites two counter-propagating magnetosonic modes, oscillating at the LF branch frequency  $\omega_{\text{LF}} \sim k_x (c_A^2 + c_s^2)^{1/2}$ . These counterpropagating magnetosonic modes are dominated by the  $\tilde{u}_x$  velocity component and account for about 1/2 of the  $u_0(x)$  initial amplitude, since that of the  $\tilde{u}_y$  component results  $\sim (k_x \rho_i / 4) \sqrt{\beta / (1 + \beta)}$  smaller. The remainder of the initial velocity profile should be carried away by the HF branch, which for small  $k_x d_i$  has a circular polarization  $\{1, -i\}$  with respect to the basis  $\{u_x, u_y\}$ . However, at the same spatial scales, the HF branch group velocity is  $v_{\text{HF}} \sim k_x d_i c_A / 2$ , which is small for  $k_x d_i \ll 1$ . This maintains the velocity shear (i.e.  $\omega_z$ , Fig. 3c) localized in a spatial interval of width  $2\Delta x / d_i \simeq 2v_{\text{HF}} \Omega_c \Delta t$ , centred around  $x/d_i \simeq 0$ , for a time interval  $\Delta t$  and explains the corresponding behaviour of the pressure anisotropies  $A^{\text{gyr}}$  and  $A^{\text{ng}}$ , which keep on staying localized close to  $x = 0$ , while oscillating at about  $\sim 2\Omega_c$  (i.e. at the frequency of the HF branch at  $k_x d_i \ll 1$ ). Also note that the broadening of the vorticity sheet related to the propagation of the wave packets takes place linearly in time with time-scales  $\omega_{\text{LF}}^{-1}$  and  $\omega_{\text{HF}}^{-1}$ , and thus more slowly with respect to the anisotropization process, even when the time-scales of the former result to be comparable to  $\tau_{\text{an}}$ , (as, for example, for the  $k_x d_i \sim 1$  spectral component of the LF branch in the numerical example considered). The fact that the broadening of the vorticity sheet is mostly due to the propagation of the large wavelength spectral component  $k_x d_i < 1$  of the LF branch is evidenced in Fig. 3 by the dashed lines, whose slope represents the inverse phase velocity of the LF branch evaluated for  $\omega_{\text{LF}} \sim k_x (c_A^2 + c_s^2)^{1/2}$ .

On the other hand, the fact that the vorticity sheet configuration is not an equilibrium condition in an initial homogeneous and isotropic plasma when an anisotropic tensor described by equation (3) is accounted for, contrasts the onset of the KH instability. Both the anisotropization and the maximally unstable KH mode grow exponentially in time over the same time-scale  $\gamma_{\text{KH}}^{-1} \sim L_H / u_y^0 \sim L_H / c_H \sim \tau_{\text{an}}$ . However, the widening of the vorticity sheet, which is self-consistently accounted for in the shear-induced anisotropization process, opposes to the onset of the KH on a time-scale essentially provided by  $\omega_{\text{LF}}^{-1}$ .

The competition between the vorticity sheet dynamics and the onset of the KH, which we have discussed in the framework of the fluid model extended to include a full pressure tensor evolution, appears to be qualitatively consistent with the results of full kinetic (PIC) numerical simulations, in particular those by Nakamura et al. (2010). They have pointed out that the dominant effect due to the kinetic modelling of a KH unstable velocity field is on the broadening of the initial velocity shear layer. While the observed broadening of an initial velocity profile  $u_y^0(x) = c_A \tanh(x/d_i)$  up to a width  $\sim 2\rho_i$  over a time  $\sim \Omega_c^{-1}$  appears to be compatible with the action of the LF branch for  $k_x d_i < 1$ , the existence of a final relaxed state cannot be interpreted in the framework of the fluid collisionless model.

## 6 DISCUSSION: VORTICITY, ANISOTROPY, AND TURBULENCE

An excellent correlation between pressure gyrotropic anisotropy and fluid vorticity has been evidenced first by Franci et al. (2016b) and then by Parashar & Matthaeus (2016), and an analogous correlation between agyrotropy and vorticity has been more recently remarked in Valentini et al. (2016). On the other hand, as we have pointed out, the fluid vorticity does not play any role in the shear-induced anisotropization mechanism, and an interpretation of the anisotropization observed in kinetic simulations of Alfvénic turbulence has been related to the deformations of the distribution function induced by electromagnetic (e.m.) effects (Valentini et al. 2016).

We now discuss (Section 6.1) how the shear-induced anisotropization mechanism, first proposed in Del Sarto et al. (2016a) as a candidate to explain the generation of anisotropy in presence of localized shear flows in developed turbulence, could provide a reasonable explanation to the aforementioned correlations.

### 6.1 Shear-induced anisotropization and plasma turbulence

The idea we pursue here is that, although e.m. effects dominate the evolution of Alfvénic turbulence in a kinetic plasma, the ‘efficient cause’ behind the observed anisotropy and identified in Valentini et al. (2017) as an ‘ion differential heating close to thin current sheets’ be in the dynamical action of *the rate of shear associated with thin vorticity sheets* on the second-order moment,  $\Pi$ , of the distribution function. This would have the appealing feature to provide an actual *mechanism* of anisotropization, which is moreover based on dynamical effects that can be described in terms of macroscopic quantities. Furthermore, as we will see, it seems to comply with many features observed in the quoted studies of numerical turbulence, and in particular with the debated role of vorticity (Franci et al. 2016b; Parashar & Matthaeus 2016; Valentini et al. 2016). This point of view appears to be confirmed by more recent kinetic simulations by Yang et al. (2017a,b).

First, we note that  $d_i$  at  $\beta \ll 1$ , and  $\rho_i$  at  $\beta \gg 1$  with cold electrons (or  $\rho_s \equiv \rho_i \sqrt{T_e/T_i}$  if the electron temperature is the dominant contribution to the plasma  $\beta \gg 1$ ), provides the order of magnitude of the characteristic shear lengths of steady structures in turbulence. An estimation of the typical scale of the thickness  $\delta$  in developed turbulence can be indeed provided by considering that for a steady vorticity/current sheet generated by turbulent motion, the condition  $\partial_t = 0$  and the balancing between the convective terms  $\sim \mathbf{u} \cdot \nabla(\dots)$  and the other terms of equations (1–5) can be assumed. The balance between the r.h.s. terms of the induction equation (5) [or equivalently between the  $\mathcal{L}_u(\Pi)$  and  $\mathcal{M}_B(\Pi)$  operators of equation (3)] gives  $L_H \sim d_i c_H / c_A$ . An analogous balance between the terms  $\mathbf{u} \cdot \nabla \mathbf{u} \sim \Omega_c \mathbf{J} \times \mathbf{b} / (ne)$  (for  $\beta \ll 1$ ) and  $\mathbf{u} \cdot \nabla \mathbf{u} \sim \nabla \cdot \Pi / (mn)$  (for  $\beta \gg 1$ ) in momentum equation (2) gives  $c_H^2 \sim c_A^2$  and  $c_H^2 \sim c_s^2$ , respectively. We can thus evaluate the characteristic layer thickness  $\delta$  as the typical scale length  $L_H$  satisfying the above estimate, so to obtain

$$\begin{aligned} \delta &\sim \rho_i \sim d_i \quad \text{when } \beta \sim 1 \quad \text{and} \\ \delta &\sim d_i \quad \text{for } \beta \ll 1, \quad \delta \sim \rho_i \quad \text{for } \beta \gg 1. \end{aligned} \quad (35)$$

The estimate  $\delta \sim \rho_s$  for  $\beta \gg 1$  follows instead when the electron temperature in equation (2) is accounted for, at the place of ion temperature. These values appear to be correlated also with the

numerical estimates of the spectral break at the ion scale, well known for  $\beta \sim 1$  to be at  $kd_i \sim 1$  (Bale et al. 2005) and recently evidenced in 2D hybrid-PIC turbulence simulations by Franci et al. (2016a) to be at  $k\rho_i \sim 1$  for  $\beta > 1$  ( $k$  being the wavevector amplitude).

On the other hand, we have shown (Section 4) that  $\delta \sim d_i$  is the characteristic thickness at which, for  $\beta \sim 1$ , the generation of non-gyrotropic and gyrotropic anisotropy occurs over a time  $\tau_H \sim \tau_B$ , and that the 1D flow sheared over a layer of thickness  $\delta \sim d_i$  is representative of a vorticity sheet in which  $\delta$  is the scale of variation across the vorticity sheet, much smaller than the scale of variation  $L$ , providing the vorticity sheet elongation.

Therefore, from the discussion of the two previous paragraphs we may conclude that the 1D flow sheared over a layer of thickness  $\delta \sim d_i$  is locally representative of the shear-driven anisotropization mechanism which can be encountered in *fluid*<sup>1</sup> turbulence at  $\beta \lesssim 1$ . As shown in Fig. 3, in this limit the gyrotropic and non-gyrotropic anisotropies  $A^{\text{gyr}}$  and  $A^{\text{ng}}$  are correlated to both the strain rate  $D_{\perp}$  and the fluid vorticity  $\omega_z$  (cf. equations 28 and 32), even if the former only intervenes in the anisotropization mechanism (equations 26 and 27). As we are going to discuss in the next subsections, where we compare this mechanism to previous interpretations of anisotropy generation in plasma turbulence, we argue that such a shear-driven anisotropization mechanism be relevant also to the regimes of Alfvénic turbulence investigated in the kinetic simulations quoted above.

## 6.2 Comparisons with previous interpretations

The generation of localized non-gyrotropic and gyrotropic ion pressure anisotropy in Alfvénic turbulence at  $\beta \sim 1$  has been first remarked by Servidio et al. (2012).

In the following part of this section, we will compare the interpretation described above for the generation of the pressure anisotropy with different interpretations that have been proposed in the literature.

### 6.2.1 Correlation between pressure anisotropy and current sheets

In Servidio et al. (2012), first, then in Perrone et al. (2013) and Servidio et al. (2015), and, more recently, in Valentini et al. (2016), a correlation has been pointed out between local peaks of  $A^{\text{ng}}$  and current density structures  $J_z$  of characteristic thickness  $\delta \sim d_i$ . In these works, where the development of 2D Alfvénic turbulence has been investigated with hybrid-Vlasov simulations, the source of anisotropy has been attributed to the turbulent character of the e.m. field and to its ‘intermittent’ features meant as spatially non-uniformities. In this context, a more specific mechanism for the generation of pressure anisotropy has been recently proposed in Valentini et al. (2017), where kinetic Alfvén waves generated by phase-mixing of shear Alfvén waves propagating in an inhomogeneous plasma have been shown to induce a deformation of the ion distribution function that leads to both agyrotropic and gyrotropic anisotropy.

<sup>1</sup> In the 2D configuration we are considering here, we can distinguish between *fluid* and *Alfvénic* turbulence, since a spatial dependence is assumed only on the coordinates  $(x, y)$  perpendicular to a background magnetic field  $\mathbf{B} = B_0 \mathbf{e}_z$ . With *fluid* we mean the turbulence achieved when perturbations are excited on the components  $u_x$  and  $u_y$  only, and not on the components of  $\mathbf{B}$  (we recall in this regard that the condition  $\mathbf{B} \times \boldsymbol{\omega} = 0$  is maintained at any time since  $\tilde{u}_z = \tilde{B}_x = \tilde{B}_y = 0$ ). 2D *Alfvénic* turbulence requires instead the excitation of both fluid  $(u_x, u_y)$  and magnetic  $(B_x, B_y)$  in-plane components.

Our interpretation differs from those which have been provided above, since we deem that the correlation between  $J_z$  and  $A^{\text{ng}}$  or  $A^{\text{gyr}}$  does not necessarily imply a casual relation. While we cannot exclude the role that e.m. effects may play in the anisotropization process, we have shown that the effect of  $J_z$  is not necessary to the anisotropization model we propose (where no  $J_z$  fluctuations are generated – cf footnote 1). We interpret instead such a correlation to be due to the shear-driven anisotropization mechanism which, as stated above, for elongated vorticity sheets appears to be correlated to (but not determined by) the fluid vorticity and to the fact that vorticity and current sheets develop close one to each other in a low collision plasma with a 2D coordinate dependence. This coincidence is essentially due to the generation of vorticity because of the rotational of the Lorentz force intervening as a source term in the vorticity equation (Matthaeus 1982), and to the convection by the fluid flow of the component of the electron canonical momentum parallel to the out-of-plane magnetic field. An example is provided by the generation of current and vorticity sheets near X-points in magnetic reconnection (Matthaeus 1982), or by the turbulence developed in the non-linear regime of strong guide field or of electron magnetohydrodynamics collisionless reconnection, where current sheets are advected by the flow along the vorticity sheets and are subject to secondary reconnecting processes in the turbulent regime achieved inside of the magnetic island (Del Sarto, Califano & Pegoraro 2003, 2005).

This point of view about the anisotropization mechanism in Alfvénic turbulence appears to be supported also by Vlasov studies (Parashar & Matthaeus 2016), where it has been evidenced that:

(i) vorticity structures are generated in a kinetic plasma, typically very close to current sheets and

(ii) that a proton heating, which depends on the local sign of  $\mathbf{B} \cdot \boldsymbol{\omega}$ , seems to be more strongly correlated to the vorticity than to the current density profile.

Further evidence in this regard has been more recently provided by the works of Yang et al. (2017a,b), which we consider as supportive of the interpretation we propose: these authors have shown by full Vlasov–Maxwell simulations of 2D Alfvénic turbulence that the action of the fluid strain  $\boldsymbol{\Sigma} = \nabla \mathbf{u}$  on  $\boldsymbol{\Pi}$  is the only one responsible for the generation of the plasma internal energy, whereas the e.m. forces contribute to the generation of localized proton and electron flows, i.e. current sheets.

Finally, the anisotropization mechanism that we describe can also qualitatively account for the fact that the gyrotropic anisotropization of alpha particles is more pronounced than that of protons, as shown by Valentini et al. (2017). Since the cyclotron frequency of alphas is half that of protons, the anisotropization due to the rate of shear  $D$  results to be more efficient for the alphas which have a value of  $\tau_B/\tau_H$  twice larger than the protons.

### 6.2.2 Correlation between pressure anisotropy and fluid vorticity

The hybrid-PIC simulations of 2D Alfvénic turbulence by Franci et al. (2016b) have first evidenced, instead, a correlation between  $A^{\text{gyr}}$  and the spatial distribution of vorticity sheets  $\omega_z$  of thickness  $\delta \sim d_i$ . This correlation, also involving the non-gyrotropic anisotropy  $A^{\text{ng}}$ , has been then rediscussed by Parashar & Matthaeus (2016) and, more recently, it has been noted by Valentini et al. (2016) and re-interpreted by Yang et al. (2017a,b). In Franci et al. (2016b), Parashar & Matthaeus (2016), and Yang et al. (2017a,b), in particular, the possible role played by the fluid vorticity in the anisotropization process has been suggested.

Our interpretation is that this correlation too is not causal, but that instead it is due to the correlation between fluid vorticity and rate of shear  $\mathbf{D}$ , the latter alone providing the mechanism of anisotropization. This has been recently reported also in Yang et al. (2017b), where the strong correlation between proton heating and vorticity has been explained, as we discuss here, as due to the fact that ‘in the large Reynolds number limit, nearby vortices are stretched to planar sheet-like structures that have equal part symmetric and anti-symmetric velocity stresses’. It has been noted however in the same work that vorticity may distort the distribution function. While further kinetic studies exist that provide similar conclusions, such as the gyrokinetic simulations of tokamak turbulence by Strugarek et al. (2013a,b), we point out that these results fall outside the extended-MHD description that we have adopted. For example the ‘fluid vorticity injection’ in Strugarek et al. (2013a,b), from which a relatively important gyrotropic temperature anisotropy follows, can be shown to correspond to a polarization density injection (Ghizzo et al. 2017b).

In concluding this section, we remark that our interpretation is not limited to configurations with imposed large aspect ratio vorticity sheets in which  $D_{\perp} \sim \omega_z/2$  (equation 28). In fact, even a flow with an initial null rate of shear  $\mathbf{D}_{\perp}$  (corresponding by itself to a quite special configuration – see Appendix A) will naturally evolve into a configuration with non-vanishing  $\mathbf{D}_{\perp}$  due to the action of the gradients of the magnetic and plasma pressure (see Appendix B).

## 7 LONG-TERM SELF-CONSISTENT E.M. EFFECTS

A long time description of the self-consistent pressure tensor evolution must take account the onset of e.m. effects.

Besides the work cited in Section 6.2.1, we have previously seen that at perpendicular propagation both magnetoacoustic waves (the LF branch) and non-electrostatic generalized ion-Bernstein waves (the HF branch) are involved in the non-linear pressure tensor dynamics, and it is known, e.g. from tokamak experiments (Amatucci et al. 1996; LeBlanc et al. 1999) that ion-Bernstein waves can generate sheared flows and vice-versa. In addition, the role played on the full pressure tensor dynamics by anisotropy-driven instabilities is not less important. The fast time-scale of the anisotropization mechanisms which can be achieved when the hydrodynamic time and length-scale approach the ion kinetic scales (that is, for values of  $\tau_H/\tau_B$  or  $\ell$  approaching unity – see equations 9 and 10) makes the process relevant to a variety of e.m. anisotropy-driven instabilities. These range from instabilities which feed on gyrotropic or non-gyrotropic pressure anisotropies by amplifying e.m. perturbations (Section 7.1, next) to reconnecting instabilities for which the change of magnetic topology is allowed or enhanced by pressure anisotropy effects (Section 7.2). Differently from the KH instability, these anisotropy-driven instabilities do not affect the stability of a vorticity sheet *per se*. However, they are likely to influence the evolution of the vorticity sheet, since they influence the persistence in time of the shear-induced anisotropy and the dynamics of the e.m. structures.

### 7.1 Anisotropy-driven e.m. instabilities feeding on pressure anisotropy

First, we consider the instabilities which can find their free energy in the pressure anisotropy generated close to a sufficiently strong local value of the rate of shear  $\mathbf{D}$  (e.g. close to a vorticity sheet). Such

instabilities can induce during the first stage of their evolution an isotropization of the plasma pressure which is even more efficient than the heat flux gradient (which is not included in our analysis – see Section 3). An example is provided by the Weibel instability, as discussed in Sarrat et al. (2016) and Ghizzo et al. (2017a), or by the fire-hose and mirror instabilities, whose thresholds are supposed to fix the boundaries, in the parameter space, of the ion gyrotropic anisotropy measured in the solar wind (Hellinger et al. 2006). In particular, the anisotropization at the electron scales should be taken into account when describing Weibel-type instabilities. In this case, electron agyrotropy (labelled  $e$  hereafter) can be expected to develop on a time-scale  $m_e/m_i$  shorter than ions (labelled  $i$  hereafter). For example, considering the  $\mathbf{B} \times \boldsymbol{\omega} = 0$  configuration and assuming comparable velocities  $c_H^e \sim c_H^i$  in the plane perpendicular to the local magnetic field implies

$$\frac{\tau_H^e}{\tau_B^e} \equiv \frac{c_H^e}{L_H^e \Omega_c^e} \sim \left( \frac{m_i}{m_e} \frac{L_H^i}{L_H^e} \right) \frac{\tau_H^i}{\tau_B^i}, \quad (36)$$

where  $\tau_H^{\alpha}/\tau_B^{\alpha}$  generalizes equation (9) for  $\alpha = e, i$ . Unless  $L_H^i/L_H^e \sim m_e/m_i$ , equation (36) implies  $\tau_H^e/\tau_B^e \gg \tau_H^i/\tau_B^i$ . Note that, for equally oriented vorticities, the different sign of the charge  $q^{\alpha}$  implies a different contribution of the anti-commutators  $[(q^{\alpha}/|q^{\alpha}|)\mathbf{B}_{\perp} + \mathbf{W}_{\perp}, \boldsymbol{\Pi}_{\perp}^{\alpha}]$  for ions and electrons (cf. equation 24 for the ion case). This affects, for example, the stability threshold of the anisotropization mechanism (cf. Section IV of Del Sarto et al. 2016a).

### 7.2 Anisotropy-driven e.m. instabilities feeding on magnetic energy

Current structures generated near the vorticity sheets during developed Alfvénic turbulence are well known to be subject to secondary reconnection events (Matthaeus & Lamkin 1985; Lazarian & Vishniac 1999), typically indicated with the name of ‘turbulent reconnection’ processes.<sup>2</sup> These have been measured in the solar wind (Retinò et al. 2011) and are expected to fundamentally contribute to the heating of the solar corona (Lazarian & Vishniac 1999; Velli et al. 2015). Due to the large-scale separation between the macroscopic scale (e.g. the simulation box size) and the turbulent current sheet structures, the models which link the global rate of magnetic energy dissipation to the local reconnection processes are clearly statistical in nature (Lazarian & Vishniac 1999). Nevertheless, they rely on specific assumptions and models for the average reconnection processes on the single current sheet. Depending on the relative amplitude of the single current sheet magnetic field with respect to the field mean reference amplitude (Del Sarto & Ottaviani 2017), these reconnecting modes are likely to develop either as standard tearing modes, or in the *ideal tearing* regime (Pucci & Velli 2014; Del Sarto et al. 2016b), as it has been evidenced by numerical studies of the stability of current sheets whose aspect ratio increases at an Alfvénic time-scale (Tenerani et al. 2015; Tenerani et al. 2017). It is in this way that pressure anisotropy effects are expected to intervene in tearing-type instabilities, which can develop on the current sheets generated by Alfvénic turbulence.

Electron agyrotropy, in particular, is expected to play a prominent role, since via a non-null  $\mathbf{B} \cdot (\nabla \times \nabla \cdot \boldsymbol{\Pi}^{(e)})$  contribution it is

<sup>2</sup>The same terming is sometimes used for the feedback of a turbulent background on large-scale tearing modes (Loureiro et al. 2009; Muraglia et al. 2009). The latter is not the case considered here, even if the role of shear-driven pressure anisotropization is of course relevant to it, too.

capable to break alone the field line connection of ideal MHD (Vasyliunas 1975; Axford 1983), as resistivity and electron inertia do. Ion agyrotropy formally does the same but with a contribution  $m_e/m_i$  smaller in amplitude in non-ideal Ohm's law, which combines with the relatively slower anisotropization rate expected from equation (36). Both species agyrotropies are however known from hybrid-PIC (Hesse & Winske 1993) and PIC (Cai & Lee 1997) simulations to play a dominant role in the acceleration of ions and electrons along the  $X$ -line (i.e. the  $z$  direction, in the 2D case considered here). Furthermore, the gyrotropic anisotropy of both species strongly influences the linear and non-linear tearing mode reconnection rate. On the one hand, indeed, the difference between the parallel and perpendicular pressure in a CGL closure, despite not contributing to the parallel component of generalized Ohm's law, modifies the  $\Delta'$  instability parameter of tearing modes in strong guide field, low- $\beta$  plasmas: for  $\hat{A}^{\text{gyr}} < 1$ , it leads to a faster reconnection rate and shifts the instability threshold at larger wavenumbers, whereas it stabilizes the reconnecting mode when  $\hat{A}^{\text{gyr}} > 1$  (Chen & Palmadesso 1984). On the other hand, it has been recently pointed out by Cassak et al. (2015) that the electron gyrotropic anisotropy, self-generated in a CGL gyrotropic closure in the neighbourhood of an  $X$ -point, may be a dominant effect for the reconnection rate increase in slab reconnection at moderate values of the plasma  $\beta$ , which is related to the dispersive features acquired by the e.m. waves propagating during reconnection. The generation and/or increase of a gyrotropic anisotropy close to a current sheet due to the different evolution of  $P_{\parallel}$  and  $P_{\perp}$  in a double adiabatic closure had been earlier studied by Vainshtein & Mazur (1982) and in several further works. In general, the occurrence of an even more complex scenario has been evidenced, when the gyrotropic ion pressure anisotropy, initial or achieved, becomes capable of destabilizing further anisotropy-driven modes such as those discussed in Section 7.1. We also remark, in this regard, that as an  $X$ -point forms on a current sheet, a further generation of both  $A^{\text{ng}}$  and  $A^{\text{gyr}}$  is expected because of the 2D traceless rate of shear  $\mathbf{D}_{\perp}$  associated with the hyperbolic flow near the  $X$ -point [this agrees with the generation of 'particle gyroviscosity' at an  $X$ -point, first suggested by Dungey 1988 (see also Dungey 1994) and more recently reformulated by Brackbill 2011].

## 8 CONCLUSION

By recalling the role played by the traceless rate of shear (Section 3) and by evidencing how this shear rate can be correlated with the fluid vorticity, we have discussed a mechanism leading to the generation of both gyrotropic and non-gyrotropic pressure anisotropy on a large aspect ratio vorticity sheet (Section 4). We have recalled how the fluid vorticity alone, through its dynamical action on the pressure tensor evolution, cannot generate any kind of anisotropy, either agyrotropic or gyrotropic. The dynamics induced by the full pressure tensor evolution, which modifies a given 1D shear flow on the same time-scale of the inverse growth rate of the KH instability, has made it possible to neglect the latter in the study of the 1D shear flow configuration which approximates the large aspect ratio vorticity sheet (Section 5). In particular, the waves which can be excited in this fluid model at propagation perpendicular to a background magnetic field intervene by carrying away the initial spatial inhomogeneity, thus stabilizing the velocity configuration with respect to the KH instability and broadening the velocity shear in agreement with numerical results of PIC simulations (Nakamura et al. 2010).

We have then provided an interpretation for the correlation between pressure anisotropy and fluid vorticity, recently shown in 2D

numerical simulations of solar wind turbulence (Section 6.1), based on the anisotropization mechanism induced by the rate of shear first discussed in Del Sarto et al. (2016a). We have compared this analysis to different interpretations of kinetic numerical results available in the literature (Section 6.1,6.2).

The analytical model discussed in Section 4, being restricted to a configuration satisfying the condition  $\mathbf{B} \times \boldsymbol{\omega} = 0$  at all times, does not account however for in-plane magnetic perturbations. An extension of the model to include these effects would allow a more direct comparison with the numerical studies of Servidio et al. (2012), Franci et al. (2016b), and Valentini et al. (2016, 2017) and would require to account for further e.m. effects such as the onset of anisotropy-driven instabilities (Section 7.1) and the occurrence of secondary reconnection processes (Section 7.2). In particular, we have commented upon the role that the anisotropization, both gyrotropic and non-gyrotropic, induced by the fluid strain, should affect the reconnecting instabilities occurring on the current structures localized close to the vorticity sheets in the so-called turbulent reconnection scenario.

As discussed throughout the paper, all these features are relevant to various phenomena observed in the solar wind and, more generally, to the physics of the heliosphere. The extension of this analysis to include the parallel fluid dynamics in a 3D coordinate dependence on the one hand, and to the simultaneous accounting of both ion and electron pressure tensors on the other hand, are the next steps to be accomplished in order for the proposed model to allow a throughout comparison with *in situ* satellite measurements such as those of Astudillo et al. (1996), Posner et al. (2003), Graham et al. (2017), He et al. (2015), and Scudder et al. (2012). This is an issue of uttermost importance, for example, to the THOR mission project (Vaivads et al. 2017) or to the study of magnetic energy dissipation by turbulent processes in the solar corona (Velli et al. 2015; Fox et al. 2016).

## ACKNOWLEDGEMENTS

We acknowledge stimulating discussions had on this subject with Matteo Faganello, Petr Hellinger, Lorenzo Matteini, William Matthaeus, Thierry Passot, Claudia Rossi, and Sergio Servidio during the *5th Vlasovia workshop* (Copanello, Italy, 2016) and the *2016 Arcetri workshop on plasma astrophysics* (Firenze, Italy, 2016). Interesting discussions with Luca Franci, Simone Landi, and Maurizio Ottaviani on the current sheet dynamics and turbulent reconnection are also gratefully acknowledged. We thank the FR-FCM for financial support through the project '*Evolution of current sheets in low-collision plasmas*' – APP 2016.

## REFERENCES

- Amatucci W., Walker D. N., Ganguli G., Antoniadis J. A., Duncan D., Bowles J. H., Gavrishchaka V., Koepke M. E., 1996, *Phys. Rev. Lett.*, 77, 1978
- Astudillo H., Livi S., Marsch E., Rosenbauer H., 1996, *J. Geophys. Res.*, 101, 24423
- Axford W. I., 1983, in Hones E., ed., *Geophysical Monograph Series, Magnetic Reconnection in Space and Laboratory Plasma*. AGU, Washington, DC, p. 1
- Bale S. D., Kellogg P. J., Mozer F. S., Horbury T. S., Reme H., 2005, *Phys. Rev. Lett.*, 94, 215002
- Batchelor G. K., 1967, *An Introduction to Fluid Dynamics*. Cambridge Univ. Press, Cambridge
- Brackbill J. U., 2011, *Phys. Plasmas*, 18, 032309
- Cai H. J., Lee L. C., 1997, *Phys. Plasmas*, 4, 509

- Cai D., Storey O., Neubert T., 1990, *Phys. Fluids B*, 2, 75
- Csakk P. A., Baylor R. N., Fermo R. L., Beidler M. T., Shay M. A., Swisdak M., Drake J. F., Karimabadi H., 2015, *Phys. Plasmas*, 22, 020705
- Cerri S. S., Henri P., Califano F., Del Sarto D., Faganello M., Pegoraro F., 2013, *Phys. Plasmas*, 20, 112112
- Cerri S. S., Pegoraro F., Califano F., Del Sarto D. F. J., 2014, *Phys. Plasmas*, 21, 112109
- Chen J., Palmadesso P., 1984, *Phys. Fluids*, 27, 1198
- Chew G. F., Goldberger M. L., Low F. E., 1956, *Proc. R. Soc. A*, 236, 112
- Chust T., Belmont G., 2006, *Phys. Plasmas*, 13, 012506
- Del Sarto D., Califano F., Pegoraro F., 2003, *Phys. Rev. Lett.*, 91, 235001
- Del Sarto D., Califano F., Pegoraro F., 2005, *Phys. Plasmas*, 12, 012317
- Del Sarto D., Pegoraro F., Califano F., 2016a, *Phys. Rev. E*, 93, 053203
- Del Sarto D., Pucci F., Tenerani A., Velli M., 2016b, *J. Geophys. Res. Space Phys.*, 121, 1857
- Del Sarto D., Ottaviani M., 2017, *Phys. Plasmas*, 24, 012102
- Del Sarto D., Pegoraro F., Tenerani A., 2017, *Plasma Phys. Control. Fusion*, 59, 045002
- Dungey J. W., 1988, in *ESA SP-285, Reconnection in space plasma: proceedings of an international workshop*, Vol. II. ESA, Noordwijk, p. 15
- Dungey J. W., 1994, *J. Geophys. Res. Space Phys.*, 99, 189
- Fox N. J. et al., 2016, *Space Sci. Rev.*, 204, 7
- Franci L., Landi S., Matteini L., Verdini A., Hellinger P., 2016a, *ApJ*, 833, 91
- Franci L., Hellinger P., Matteini L., Verdini A., Landi S., 2016b, in Wang L., Bruno R., Möbius E., Vourlidas A., Zank G., eds, *Solar Wind 14*. AIP Publishing LCC, p. 04003
- Ghizzo A., Sarrat M., Del Sarto D., 2017a, *J. Plasma Phys.*, 83, 705830101
- Ghizzo A., Del Sarto D., Palermo F., Biancalani A., 2017b, *EuroPhys. Lett.*, 119, 15003
- Graham D. B. et al., 2017, *Phys. Rev. Lett.*, 119, 025101
- Hasegawa H., Fujimoto M., Phan T.-D., Rème H., Balogh A., Dunlop M. W., Hashimoto C. R. T., 1996, *Nature*, 430, 2907
- He J., Wang L., Tu C., Marsch E., Zong Q., 2015, *ApJ*, 800, L31
- Hellinger P., Trávníček P., Kasper J., Lazarus A., 2006, *Geophys. Res. Lett.*, 33, L09101
- Hesse M., Winske D., 1993, *Geophys. Res. Lett.*, 95, 20903
- Huba J. D., 1996, *Geophys. Res. Lett.*, 23, 755
- Kaufman A. N., 1960, *Phys. Fluids*, 3, 610
- Lazarian A., Vishniac E. T., 1999, *Astrophys. J.*, 517, 700
- LeBlanc B. P. et al., 1999, *Phys. Rev. Lett.*, 82, 331
- Loureiro N. F., Uzdensky D. A., Schekochihin A. A., Cowley S. C., Yousef T. A., 2009, *MNRAS*, 399, L146
- MacMahon A. B., 1965, *Phys. Fluids*, 8, 1840
- Matteini L., Hellinger P., Landi S., Trávníček P. M., Velli M., 2012, *Space Sci. Rev.*, 172, 373
- Matthaeus W. H., 1982, *Geophys. Res. Lett.*, 9, 660
- Matthaeus W. H., Lamkin S. L., 1985, *Phys. Fluids*, 28, 303
- Mikhailovskii A. B., Smolyakov A. I., 1985, *Sov. Phys. - JETP*, 61, 109
- Muraglia M., Agullo O., Benkadda S., Garbet X., Beyer P., Sen A., 2009, *Phys. Rev. Lett.*, 103, 145001
- Nakamura T. K., Hasegawa H., Shinohara I., 2010, *Phys. Plasmas*, 17, 042119
- Parashar T. N., Matthaeus W. H., 2016, *ApJ*, 526, 697
- Perrone D., Valentini F., Servidio S., Dalena S., Veltri P., 2013, *ApJ*, 762, 99
- Plihon N. et al., 2015, *J. Plasma Phys.*, 81, 345810102
- Posner A., Liemohn M. W., Zurbuchen T. H., 2003, *Geophys. Res. Lett.*, 30, 6
- Pucci F., Velli M., 2014, *ApJ*, 780, L19
- Retinò A., Sundkvist D., Vaivads A., Mozer F., André M., Owen C. J., 2011, *Nature Phys.*, 3, 235
- Sarrat M., Del Sarto D., Ghizzo A., 2016, *Europhys. Lett.*, 115, 45001
- Schekochihin A., Cowley S. C., Kulsrud R. M., Rosin M. S., Heinemann T., 2008, *Phys. Rev. Lett.*, 100, 081301
- Scudder J. D., Daughton W., 2008, *J. Geophys. Res. Space Phys.*, 113, A06222
- Scudder J. D., Holdaway R. D., Daughton W. S., Roytershteyn V., Russell C. T., Lopez J. Y., 2012, *Phys. Rev. Lett.*, 108, 225002
- Scudder J. D., Karimabadi H., Daughton W., Roytershteyn V., 2015, *Phys. Plasmas*, 22, 101204
- Servidio S., Valentini F., Califano F., Veltri P., 2012, *Phys. Rev. Lett.*, 108, 045001
- Servidio S., Valentini F., Perrone D., Greco A., Califano F., Matthaeus W., Veltri P., 2015, *J. Plasma Phys.*, 81, 325810107
- Strugarek A. et al., 2013a, *Plasma Phys. Control. Fusion*, 55, 074013
- Strugarek A. et al., 2013b, *Phys. Rev. Lett.*, 111, 145001
- Sulem P. L., Passot T., 2015, *J. Plasma Phys.*, 81, 325810103
- Tenerani A., Velli M., Rappazzo A. F., Pucci F., 2015, *ApJ*, 813, L32
- Tenerani A., Velli M., Pucci F., Landi S., Rappazzo A. F., 2017, *J. Plasma Phys.*, 82, 53582051
- Vainshtein S. I., Mazur V. A., 1982, *Plasma Phys.*, 24, 965
- Vaivads A. et al., 2017, *J. Plasma Phys.*, 82, 125001
- Valentini F. et al., 2016, *New J. Phys.*, 18, 125001
- Valentini F., Vásconez C., Pezzi O., Servidio S., Malara F., Pucci F., 2017, *A&A*, 599, A8
- Vasyliunas V. M., 1975, *Rev. Geophys.*, 13, 303
- Velli M., Pucci F., Rappazzo F., Tenerani A., 2015, *Phil. Trans. R. Soc. A*, 373, 20140262
- Yang Y. et al., 2017a, *Phys. Plasmas*, 24, 072306
- Yang Y. et al., 2017b, *Phys. Rev. E*, 95, 061201

## APPENDIX A: EXAMPLES OF FLOWS WITH NULL RATE OF SHEAR

An incompressible, pure vortical flow with  $\mathbf{D}_\perp = 0$  necessarily corresponds to a stream function  $\varphi(x, y)$ , where both  $x$  and  $y$  have the *same* scale variation length  $a$ . To show this, we generalize the sheared flow  $\mathbf{u} = (0, u_y(x), 0)$  by adding a potential  $\psi(x, y)$  while looking at solutions of the form  $u_x(x, y) = \partial_x \psi$  and  $u_y(x, y) = V(x) + \partial_y \psi$ , which satisfy  $D_{\perp, ij} = 0 \forall i, j = x, y$ , with  $\mathbf{D}_\perp$  defined as in equation (23). In order to satisfy  $D_{\perp, xy} = D_{\perp, yx} = 0$ , the velocity potential must be of the form

$$\psi(x, y) = -\frac{1}{2}yV(x) + A(x) + B(y). \quad (\text{A1})$$

The further condition  $D_{\perp, xx} = D_{\perp, yy} = 0$  imposes a constraint on the arbitrary functions  $A(x)$  and  $B(y)$ , that is

$$\frac{d^2}{dx^2}A(x) - \frac{1}{2}y\frac{d^2}{dx^2}V(x) = \frac{d^2}{dy^2}B(y). \quad (\text{A2})$$

Differentiation of (A2) with respect to  $y$  fixes the condition  $d^2V/dx^2 = V_2$ , constant with respect to both  $x$  and  $y$ . Direct integration then gives  $V = V_0 + V_1x + V_2x^2/2$ ,  $A = A_0 + A_1x + B_2x^2/2$ ,  $B = B_0 + B_1y + B_2y^2/2 - V_2y^3/12$ , where  $A_i, B_i$ , and  $V_i$  for  $i = 0, 1, 2$  are free coefficients. Substituting in equation (A1), we obtain

$$u_x(x, y) = A_1 + B_2x - \frac{V_1}{2}y - \frac{V_2}{2}xy, \quad (\text{A3})$$

$$u_y(x, y) = \frac{V_0}{2} + B_1 + \frac{V_1}{2}x + B_2y + \frac{V_2}{4}(x^2 - y^2).$$

This flow has  $\mathbf{D}_\perp = 0$ , compression rate  $\mathcal{C}_\perp = -B_2 - V_1y/2$ , and vorticity given by  $\omega_z = (V_1 + V_2x)/2$ . Its compressionless limit  $B_2 = V_1 = 0$  leads to a stream function with circular contour levels,

$$\varphi(x, y) = -\frac{V_1}{4} \left[ \left( x + \frac{V_0 + 2B_1}{V_1} \right)^2 + \left( y - \frac{2A_1}{V_1} \right)^2 \right]. \quad (\text{A4})$$

It is important to notice that the requirement that  $x$  and  $y$  vary over the same characteristic length-scale, needed for equations (A3) to satisfy  $D_{ij} = 0$ , does not qualify these vector fields nor the stream function of equation (A4) as representative of a vorticity sheet, as it has been considered in Section 4.

**APPENDIX B: EVOLUTION OF THE RATE OF SHEAR**

The equation for the evolution of  $D_{\perp, ij}$  is obtained from the components of equations (2), combined according to the definition of equation (23). Using the total time derivative as in equations (27), expressing the in-plane strain tensor  $\partial_i u_j$  with  $i, j = x, y$  in terms of the operators  $\mathcal{C}_{\perp}$ ,  $D_{\perp, ij}$ , and  $W_{\perp, ij}$  (cf. equations 13, 22 and 23), and using the continuity equation (1), we find

$$\frac{d}{dt} \left( \frac{D_{ij}}{n} \right) = \frac{1}{2} \left( \frac{\partial^2 M_{mj}}{\partial x_i \partial x_m} + \frac{\partial^2 M_{im}}{\partial x_m \partial x_j} - \frac{\partial^2 M_{km}}{\partial x_k \partial x_m} \delta_{ij} \right), \quad (\text{B1})$$

where the r.h.s. term depends on the gradients of the divergence of the Maxwell stress tensor, which in this 2D geometry with  $\mathbf{B} \times \boldsymbol{\omega} = 0$  reads

$$M_{ij} \equiv \frac{1}{2} |\mathbf{B}|^2 \delta_{ij} + \Pi_{ij}. \quad (\text{B2})$$

Its divergence,  $\partial_k M_{ik}$ , corresponds to the  $i$ -component of the forces at r.h.s of momentum equation (2).

Analogously, under the same conditions, for the fluid vorticity, we obtain

$$\frac{d}{dt} \left( \frac{W_{ij}}{n} \right) = \frac{1}{2} \left( \frac{\partial^2 M_{mj}}{\partial x_i \partial x_m} - \frac{\partial^2 M_{im}}{\partial x_m \partial x_j} \right). \quad (\text{B3})$$

This paper has been typeset from a  $\text{\TeX}/\text{\LaTeX}$  file prepared by the author.